Temperature-Dependent Charpy Impact Property of 3D Printed 15-5 PH Stainless Steel

Sugrim Sagar[1], Yi Zhang[1], Hyun-Hee Choi[2], Yeon-Gil Jung[2], Jing Zhang[1,*]

1. Department of Mechanical and Energy Engineering, Indiana University – Purdue University Indianapolis, Indianapolis, IN 46202, USA

2. Department of Materials Convergence and System Engineering, Changwon National University, Republic of Korea

*Corresponding author: jz29@iupui.edu

Abstract

In this study, the impact property of 3D printed 15-5 PH stainless steel was investigated at low (77 K), room (298 K), and high temperatures (723 K) using integrated experimental and modeling studies. The finite element model was based on the Johnson-Cook phenomenological material model and fracture parameters. The experimentally measured impact energies are 0.01 J/cm^2, 6.78±4.07 J/cm^2, and 50.84±3.39 J/cm^2, at the low, room, and high temperatures, respectively. The experimental and modeling predicted impact energies are in good agreement. The microstructures show that the steel exhibits a brittle behavior at low and room temperatures as indicated by a transgranular fracture, but changes to a more ductile behavior at high temperatures as illustrated by microvoid coalescence induced facture morphology.

Keywords: 3D printing; additive manufacturing; Charpy impact test; Stainless steel; Microstructure; Finite element model; Johnson-Cook model

---

This is the author's manuscript of the article published in final edited form as:

Sagar, S., Zhang, Y., Choi, H.-H., Jung, Y.-G., & Zhang, J. (2021). Temperature-dependent Charpy impact property of 3D printed 15-5 PH stainless steel. Materials Science and Technology, 37(2), 190–201. https://doi.org/10.1080/02670836.2021.1885094

1. Introduction

Temperature-dependent impact properties are important because of the ductile-to-brittle response of metals from high to low temperature as exemplified by the failure of the Liberty ships in World War II [1]. The impact performance of the materials is also critical to determining applications in high strain rate deformation applications, e.g., ballistics or crashworthiness [2] and [3]. To date, there is limited published data on the impact properties of 3D printed 15-5 precipitation-hardening (PH) stainless steel; especially at cryogenic and high temperatures. The study by Pitrmuc [4] and Hendrickson [5] on 3D printed 316L stainless steel sample at room temperature shows the impact energy of 136.0 J/cm^2 for horizontal built and 41.2 J/cm^2 for a vertical build. Furthermore, at room temperature, Sistiaga [6] has found that the impact energy to be 119.5 J/cm^2 using horizontal build using selective laser sintering, whereas the conventionally manufactured equivalent is 103 J/cm^2. Therefore, previous research has been focused on the effects of 3D printing technique, process parameters and printing orientation rather than specimen temperature effect on the impact energy of 3D printed stainless steel.

For 15-5 PH stainless steel, the as-received wrought 15-5 PH stainless steel has the impact energy values of 57.2 and 46.7 J/cm^2 at the room-temperature and 219 K, respectively. For the wrought steel heat treated at 900 F (755 K), the impact energy values are 50.0 and 41.3 J/cm^2 for room-temperature and 219 K, respectively [7]. The DBTT diagrams for 15-5 stainless steel were measured in Ref.[8]. For the unaged steel, the DBTT is around 273 K, and the impact energy values are 25 and 150 J/cm^2 at the brittle and ductile regions, respectively.

For the previous impact modeling studies, Amini *et al.* developed an LS-DYNA model to simulate the response of monolithic DH-36 steel plates and bilayer steel-polyurea plates under impulsive

loads [9]. The transient response of the plates under impulsive pressure loads was studied and compared well with the experimentally observed results[9]. Barauskas *et al.* conducted the computational analysis of the impact of a bullet against the multilayer fabrics in LS-DYNA [10]. To avoid the direct modeling of filaments comprising the yarns, the yarns were modeled by using thin shell elements[10].

This paper presents a combined experimental and finite element modeling study to investigate the temperature-dependent Charpy impact property of 3D printed 15-5 PH stainless steel. The paper is arranged as follows: Section 2 provides the details of the specimen preparation and Charpy impact experiment. Section 3 presents the details of the finite element model for simulating the Charpy impact test. Section 4 gives the experimental and modeling results, and Section 5 summarizes the conclusions.

2. Experimental procedure

2.1 Sample preparation

The geometry of the Charpy impact specimens follows the ASTM E23-16b standard [11]. EOS stainless steel PH1 powder (average particle size of 20 μm) was used in this study to produce the 3D printed Charpy test specimens. The specimens were fabricated by the laser powder bed fusion (PBF) process using an EOSINT M270 machine (EOS GmbH Electro Optical Systems, Germany) equipped with a 200 W single-mode Ytterbium fiber laser at 1070 nm wavelength. The processing setting parameters include the laser power of 170 W, scanning speed of 1250 mm/s in the continuous wavelength mode, hatch spacing of 100 μm, and layer thickness of 30 μm. The laser

beam spot size is ~50 μm in diameter. Three samples were printed for each of the 77 K, 298 K, and 723 K specimens that were prepared similar to the procedure detailed in Ref. [12].

2.2 Charpy impact test

Before the Charpy impact test, the samples were placed at room temperature, high-temperature furnace, and liquid nitrogen to achieve the desired testing temperatures. For the low-temperature test, the specimens were subjected to cryogenic temperature using liquid nitrogen for 10 min until the temperature was reduced to 77 K before testing. Similarly, the high-temperature specimens were placed in an oven for 15 min and heated to 1000 K to ensure that the target temperature of 723 K was achieved immediately before testing. The Charpy impact test was undertaken similar to [12].

3. Numerical modeling

3.1 Finite element model

The geometry of the Charpy impact specimens follows the ASTM E23-16b standard. The CAD file in iges format consisting of the striker, specimen, and anvil parts were imported into the structural simulation software LS-PREPOST/LS-DYNA [13] and meshed using solid elements. Further mesh refinement was executed on the specimen at the impact zone as shown in Fig. 1.

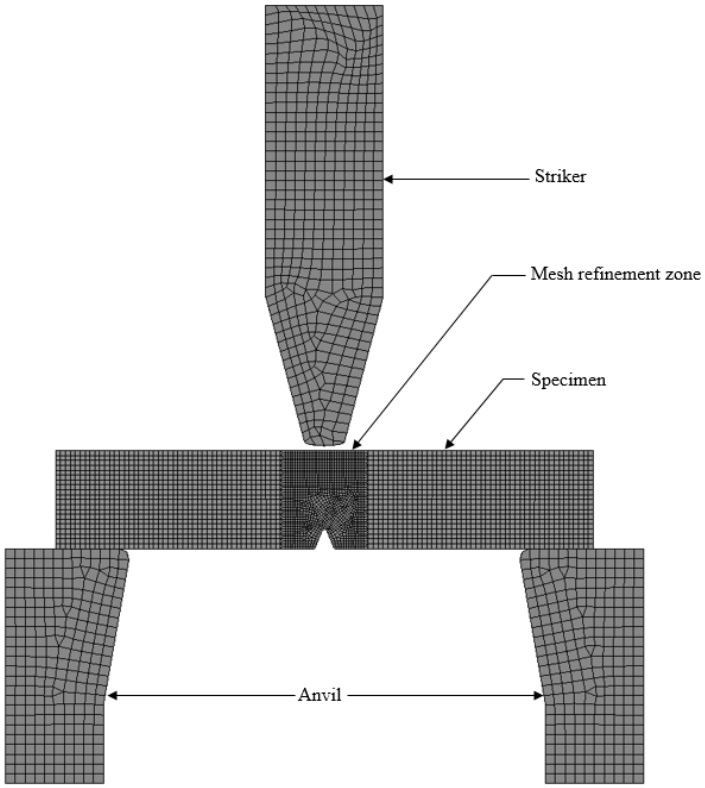

Figure 1: Finite element model and mesh of striker, specimen, and anvil.

Rigid body properties were assigned on the striker and anvil in order to simulate experimental test conditions and to mitigate against kinetic energy loss through the impacting and support structures. Sliding contact conditions were assigned to the specimen/anvil and striker/specimen interfaces.

Given that the mass of the striker used in the Charpy impact experiment was 30.24 kg, an adjustment of the density based on the revised geometry was necessary. The volume of the striker is 6212.99 mm^3; hence the adjusted density is $4.87e^{-3}$ kg/mm^3.

By equating the potential energy of the dropping striker to the kinetic energy at impact, the initial velocity was calculated using $v = \sqrt{2gh}$. The height, h was determined from the experimental Charpy impact test i.e. 1.366 m, and g is the acceleration due to gravity thus yielding the initial velocity as 5.18 m/s.

The mesh refinement was undertaken by creating a shell element out of a solid face (side), followed by further refining the mesh within the impact zone. Triangular meshes were created to transition the connection between the larger mesh with the refined zone. A solid mesh was achieved by shell dragging through a compartmentalized extrusion through the thickness of the specimen. The brick solid mesh was used in preference to tetrahedral mesh because of better accuracy per mesh size for high strain rate application. Some tetra mesh types exhibit volumetric locking which results in a more rigid response, further refinement results in no additional increased accuracy, but with the consequence of higher demand for computing resources.

The distance between the striker and specimen was assigned a relatively close distance, i.e., 1.0 mm in order to reduce analysis time. The Flanagan-Belytschko integration hourglass-control algorithm is used to damp out the overall zero-energy modes.

3.2 Johnson-Cook constitutive material model

In order to capture the high strain rate response of the specimen, the Johnson-Cook (J-C) phenomenological constitutive model [14] was used. The J-C is a flow stress model that consists of strain hardening, strain-rate, and thermal softening components as shown in Eq. (1).

$$\sigma_{eff} = \underbrace{\left(A + B\bar{\varepsilon}^{p^n}\right)}_{\text{Strain hardening}} \overbrace{\left[1 + Cln\left(\frac{\dot{\bar{\varepsilon}}^p}{\dot{\varepsilon}_0}\right)\right]}^{\text{Strain-rate effects}} \underbrace{\left[1 - \left(\frac{T - T_r}{T_{melt} - T_r}\right)^m\right]}_{\text{Thermal softening}} \quad (1)$$

where the parameters are defined as follows: σ_{eff} effect stress, A plastic yield stress, B plastic hardening parameter, C strain rate coefficient, n plastic hardening exponent, m temperature softening exponent, $\bar{\varepsilon}^p$ effective plastic strain, $\left(\frac{\dot{\bar{\varepsilon}}^p}{\dot{\varepsilon}_0}\right)$ dimensionless plastic strain rate where $\dot{\varepsilon}_0$ and $\dot{\bar{\varepsilon}}^p$ represents reference and effective the plastic strain rates respectively, and $\left(\frac{T-T_r}{T_{melt}-T_r}\right)$ the dimensionless homologous temperature, in which, T, T_r and T_{melt} are the initial, reference, and melting temperatures respectively.

The temperature softening expression shown in Eq. (1), represents the effect on flow stress due to the adiabatic condition caused by plastic work of deformation. The reference temperature, T_r represents the temperature of the specimen before testing i.e. 77 K, 298 K, and 723 K, whereas the initial temperature, T represents the temperature after impact and is due to adiabatic heating. The maximum reference temperature, T_r was significantly lower than the melting temperature of the specimen, T_{melt} because of the uncertainty of the accuracy of the J-C constitutive model in predicting the behavior of the specimen at the near-melting point.

Since the J-C constitutive material model for 3D printed 15-5 PH stainless steel parameters were not readily available, the wrought equivalent presented in [15] were used in this study. The values of A, B, C, n, and m were each investigated for T_r values of 77 K, 298 K and 723 K in the LS-DYNA model to match the behavior of the experimental Charpy impact test; however, the effect of each constitutive model parameter on the impact energy was found to be negligible. More accurate values of each parameter may be explored using the torsion test, dynamic Hopkinson bar test, and tensile tests over a range of temperatures [14]. The J-C parameters used for defining the material properties of the specimen are presented in Table 1.

Table 1: Johnson-Cook constitutive model parameters for 15-5 PH stainless steel.

J-C model parameter used in Eq. (1)	Value
A	855 MPa
B	448 MPa
C	0.014
n	0.14
m	0.63
$\dot{\varepsilon}_0$	1.0 s-1
T_{melt}	1713 K
T_r (1) Low temperature (2) Room temperature (3) High temperature	 77 K 298 K 723 K

It is noted that the same J-C model parameters for the wrought material (Table 1) were used in this study. However, a different set of parameters for the damage model were used for the 3D printed stainless steel (Table 2).

3.3 Johnson-Cook fracture parameters

In order to model the fracture and failure characteristics beyond plastic deformation, the Johnson-Cook (J-C) failure criteria [16] was used. A fracture occurs when the following fracture parameter, D, reaches unity as shown in Eq. (2):

$$D = \sum \frac{\Delta \bar{\varepsilon}^p}{\varepsilon^f} \tag{2}$$

where $\Delta \bar{\varepsilon}^p$ is the increment of equivalent plastic strain, and ε^f is the equivalent strain at failure under given conditions defined by Eq. (3):

$$\varepsilon^f = \underbrace{\left[D_1 + D_2 \exp D_3 \left(\frac{p}{\sigma_{eff}}\right)\right]}_{\text{Strain hardening dependence}} \overbrace{\left[1 + D_4 \ln\left(\frac{\dot{\bar{\varepsilon}}^p}{\dot{\varepsilon}_0}\right)\right]}^{\text{Strain-rate dependence}} \underbrace{\left[1 + D_5 \left(\frac{T - T_r}{T_{melt} - T_r}\right)\right]}_{\text{Temperature dependence}} \tag{3}$$

where the parameters are defined as follows: D_1 initial failure strain, D_2 exponential factor, D_3 triaxiality factor, D_4 strain rate factor, D_5 temperature factor, $\left(\frac{p}{\sigma_{eff}}\right)$ triaxiality ratio, where p and σ_{eff} represent the hydrostatic pressure and effective stress respectively. The input parameters $D_1 \sim D_5$ are material failure dimensionless parameters that are experimentally determined from the torsion test over a range of strain rates, Hopkinson bar test over a series of temperatures, and quasi-static tensile test over an assortment of notched specimens.

The J-C fracture model parameters, $D_1 \sim D_3$ for the 3D printed 15-5 PH stainless steel were extracted from Ref. [17]. The fracture parameters D_4 and D_5 were derived from [16] given the similar fracture mechanism as AISI 4340 steel.

By keeping the J-C constitutive material parameters and fracture parameters $D_2 \sim D_5$ constant, the numerical iterations indicated that the impact energy was mostly affected by D_1. The optimized values of D_1 corresponding to T_r values of 77 K, 298 K, and 723 K were -0.600, -0.193, and -0.143 respectively. The damage parameters along with their references used for the Charpy impact test simulation are presented in Table 2.

Table 2: Damage parameters for 3D printed 15-5 PH stainless steel.

Damage parameter used in Eq (3)	Value
D_1 (1) @ Low temperature 77 K (2) @ Room temperature 298 K (3) @ High temperature 723 K	 -0.600 -0.193 -0.143
D_2	3.810 [18]
D_3	-1.847 [18]
D_4	0.002 [18]
D_5	0.610 [18]

A linear polynomial equation of state was selected for the Johnson-Cook material model. Also, in order to activate the material model, the bulk modulus, C1 (169.1 GPa) were placed in the input card while C2 ~ C5 were set to zero.

3.4 Physical and mechanical properties

The physical and mechanical properties of 3D printed 15-5 PH stainless steel adopted from [15] are shown in Table 3.

Table 3: Physical and mechanical properties of 3D printed 15-5 PH stainless steel [15].

Material property	Value
Density, ρ	7850 kg/m^3
Young's Modulus, E	212 GPa
Poisson's Ratio, υ	0.291
Shear Modulus, G	149.5 GPa

4. Results and discussion

4.1 Microstructures of the printed samples at various temperatures

Before the Charpy impact test, the sample was placed at room temperature, furnace, and liquid nitrogen to achieve the desired testing temperatures. Different temperatures affect the microstructure and the mechanical properties of the stainless steel including its ductility and fracture toughness. Microstructures of the specimen cross-sections were characterized using optical microscopy (OM) and scanning electron microscopy (SEM).

The optical microscopic images of three samples at 77 K, 298 K, and 723 K are shown in Fig. 2. All of the three samples show dense microstructure with high relative densities (>99%), with very few pores.

As shown in Fig. 2, the austenite phase is evident. The average grain size is determined to be ~5 μm, following ASTM E112 – 13 standard. The grain size in this study is similar to the reported grain size 6.7~5.6 μm in Ref.[19].

The surface textures of room temperature and low-temperature samples are very similar, except that the room temperature one has a few visible pores (Fig. 2b). When heat-treated at high temperatures, large grains are formed (Fig.2c), an indication of grain growth at high temperatures. The high-temperature heat treatment acted as an annealing process so that the crystal lattice may relax and more ordered grains are formed.

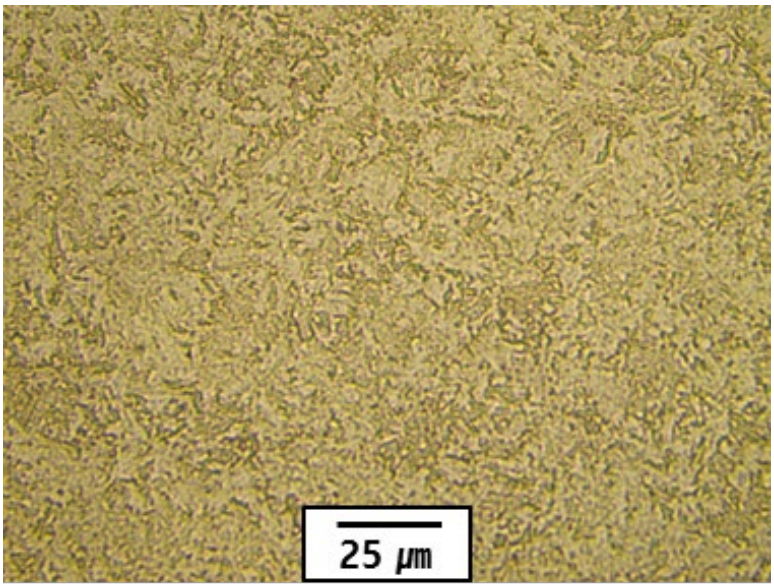

(a)

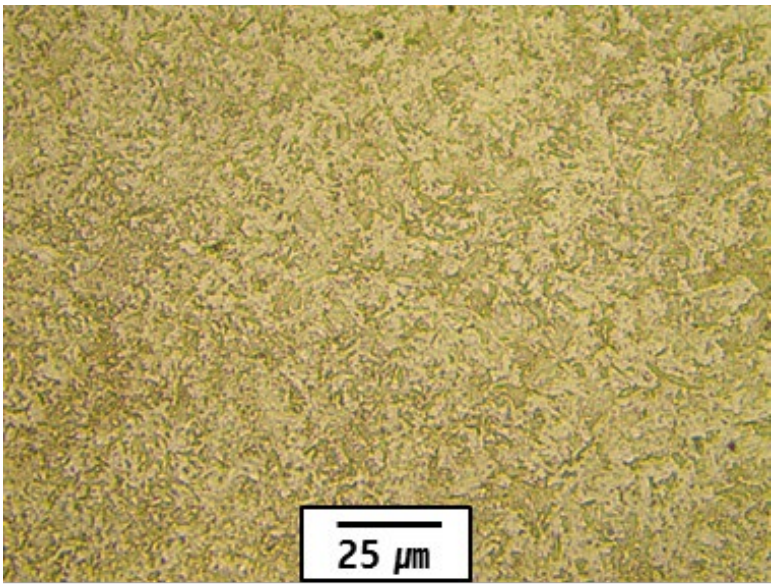

(b)

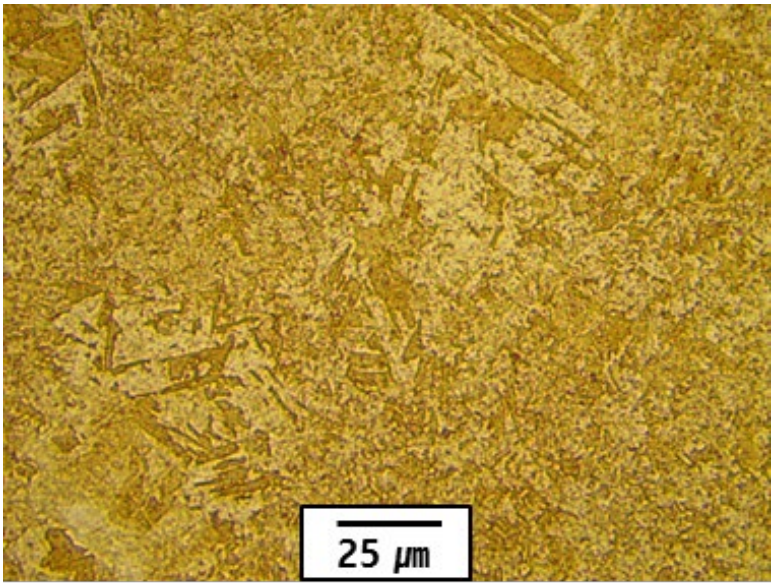

(c)

Figure 2: Optical micrographs of sample cross-sections of 3D printed 15-5 PH stainless steel at (a) 77 K, (b) 298 K, and (c) 723 K.

Detailed microstructures are revealed by the SEM images as shown in Fig. 3. At room temperature (Fig. 3b), irregularly shaped lack-of-fusion pores are observed due to the insufficient heating by laser source during the powder bed fusion process. When the as-printed sample is subjected to furnace heat treatment, the high temperature acts in two ways: increase material diffusion rate and lead to thermal expansion. The surface of the high-temperature sample (Fig. 3c) is smoother, which indicates that the rough surface is flattened by material diffusion at high temperatures. The black spots in Fig. 3c are pores, as the result of the residual pores and unmelt particles in the powder bed fusion metal 3D printing process. On the other hand, due to the thermal expansion, the compressed materials near the pore move toward the pore centers, which makes the pore size smaller, and the pore becomes to be circular. At low temperatures, because the diffusion rate is much lower, the structural change is minimum, therefore the configuration is similar to the room temperature.

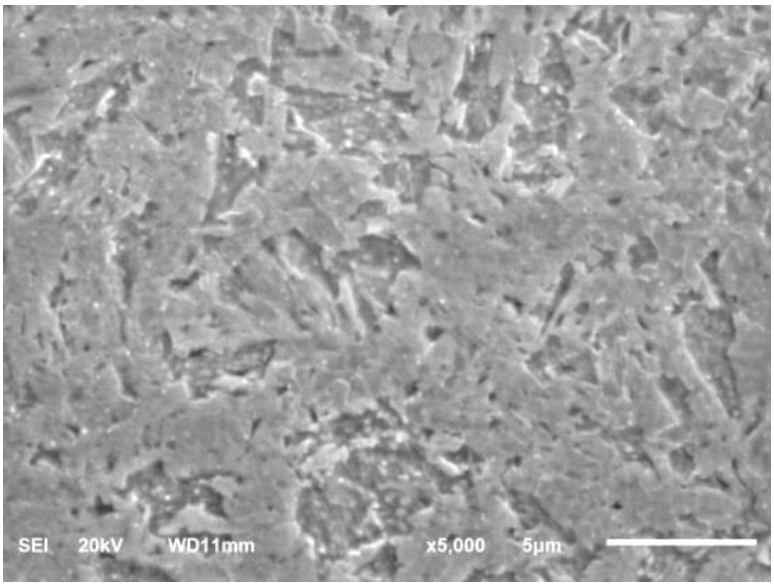

(a)

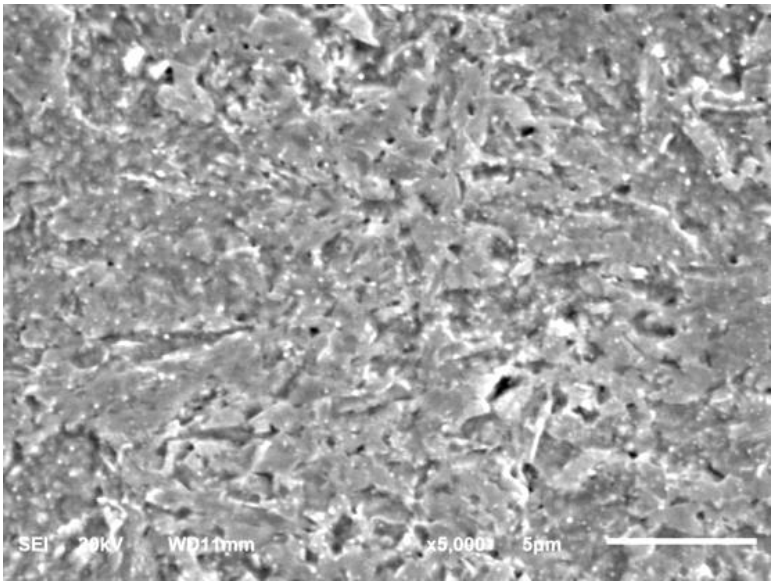

(b)

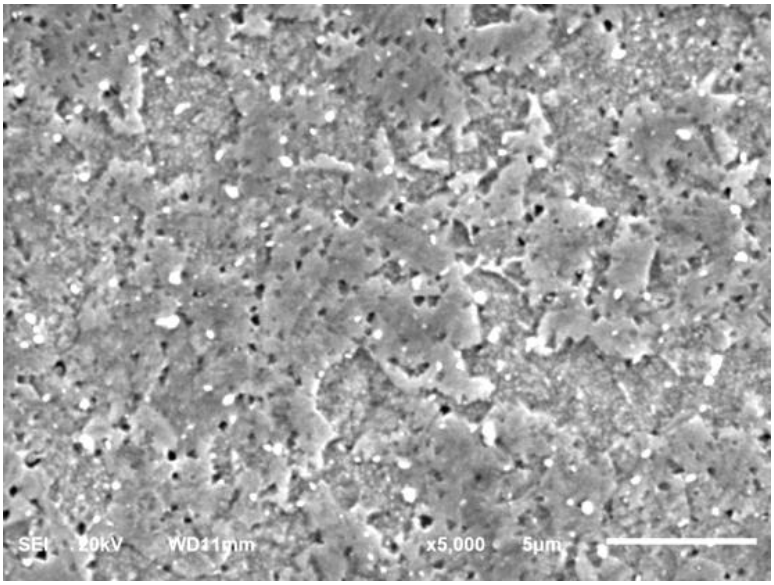

(c)

Figure 3: SEM images of the sample cross-sections at (a) 77 K, (b) 298 K, and (c) 723 K. (Scale bars represent 5 μm)

The microstructural evaluation suggests that the 3D printed samples are martensitic, which is consistent with the images reported in Ref. [20]. After high-temperature homogenization treatment,

the austenite microstructure undergoes a martensitic transformation during the subsequent quench giving rise to the formation of martensite laths inside the former austenite grains [20]. This martensitic structure is present after the precipitation treatment [20], similar to the one shown in Fig. 2c in this study.

In addition to cross-sectional micrographic analysis, the element composition of samples at three different temperatures were determined using energy-dispersive X-Ray spectroscopy (EDX). The measured element distributions of the three temperatures are shown in Table 4. Although they were tested under different temperature, the element compositions are almost identical with very slight differences. For all the three cases, Fe (75.85%-76.06%), Cr (14.80%-14.82%), Ni (4.20%-4.31%), and Cu (3.50%-3.53%) are the four major elements, Si and Nb are two minor elements that have about 1% weight percentage in total. The element weight percentages are not sensitive to temperature in this study.

Table 4: Elements in the 3D printed 15-5 PH stainless steel samples.

Element	Weight percentage (%)		
	77 K	298 K	723 K
Si	0.68	0.65	0.60
Cr	14.80	14.82	14.81
Fe	75.85	76.06	75.88
Ni	4.31	4.20	4.27
Cu	3.53	3.51	3.50
Nb	0.60	0.59	0.72

4.2 Fracture surfaces after Charpy impact test

4.2.1 Microstructure analysis of the fracture surface

After the Charpy impact test, the microstructures of the fracture surfaces were analyzed to investigate the fracture mechanisms and the material behavior under impact loading. The fracture surface micrographs of the low-temperature sample are shown in Fig. 4. For the low-temperature specimen shown in Fig. 4, a dominant transgranular or cleavage fracture morphology is evident which is usually associated with low-energy, brittle fracture caused by sources of weakness in the material [21]. The transgranular fracture or cleavage occurred along specific crystallographic planes, as shown in Fig. 4. The transgranular fracture is commonly observed in certain BCC and HCP metals, but can also occur in FCC metals when they are subjected to severe environmental conditions such as extremely high strain rates or very low temperatures[21], which is the low-temperature case in this study. The transgranular fracture or cleavage is characterized by a relatively flat fracture surface with small converging ridges [21], as shown in Fig. 4. Such a low toughness means that temperature 77 K is below the ductile-brittle transition temperature for the material. The movement of nearby atoms in the crystal lattice is suppressed by the low temperature, so that long cracks can form easily, resulting in a brittle fracture behavior, which is consistent with the recorded impact energy at low temperature is close to 0 J/cm^2.

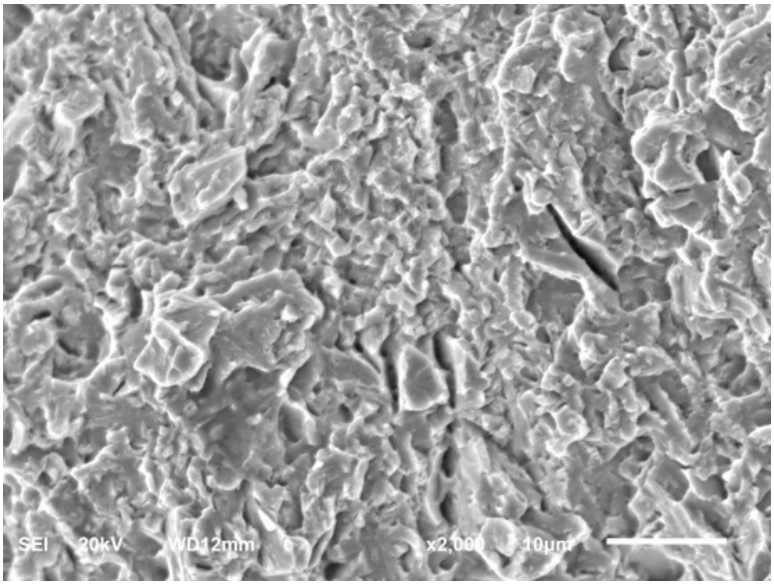

Figure 4: Scanning electron microscopic images of 15-5 PH stainless steel samples test at low temperature (77 K). (2000x magnification. The scale bars represent 10 μm).

Fig. 5 shows the fracture surface microstructure of the sample tested at room temperature (298 K). It illustrates a primary transgranular fracture with an increasingly small amount of intergranular fracture compared to the low-temperature specimen was observed. Such a microstructure suggests a brittle fracture, but with improved ductility compared to the low-temperature specimen. At room temperature, the tested impact energy is 6.78±4.07 J/cm^2. Although it is still brittle fracture at room temperature, the higher temperature increases the mobility of the lattice, and long crack propagation is partially suppressed. Therefore the impact energy is higher than that of low temperature.

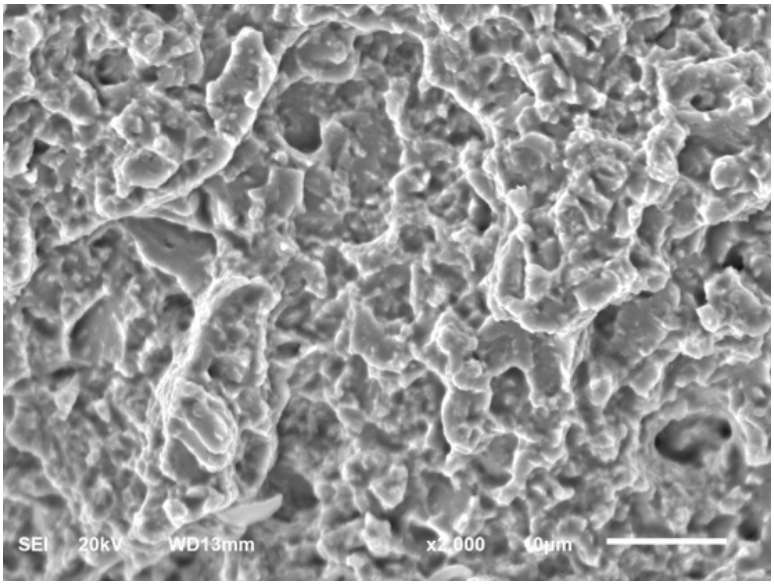

Figure 5: Scanning electron microscopic images of 15-5 PH stainless steel samples test at room temperature (298 K). (2000x magnification. The scale bars represent 10 μm).

In contrast to the low temperature specimen in Fig. 4, for the high-temperature specimen shown in Fig. 6, a more ductile fracture morphology than the low-temperature specimens was observed. The plastic deformation tends to fail by a process called microvoid coalescence (MVC) [21]. The deformation and fracture took place by the nucleation of microvoids, followed by their growth and eventual coalescence to form cracks. Fig. 6 shows the microvoid coalescence under shear loading, which leads to an elongated dimple morphology [21]. The tested impact energy, in this case, is 50.84±3.39 J/cm^2, which is the largest for three temperatures. This is because, at higher temperatures, the resistance to dislocation motion is reduced. So more impact energy can be absorbed.

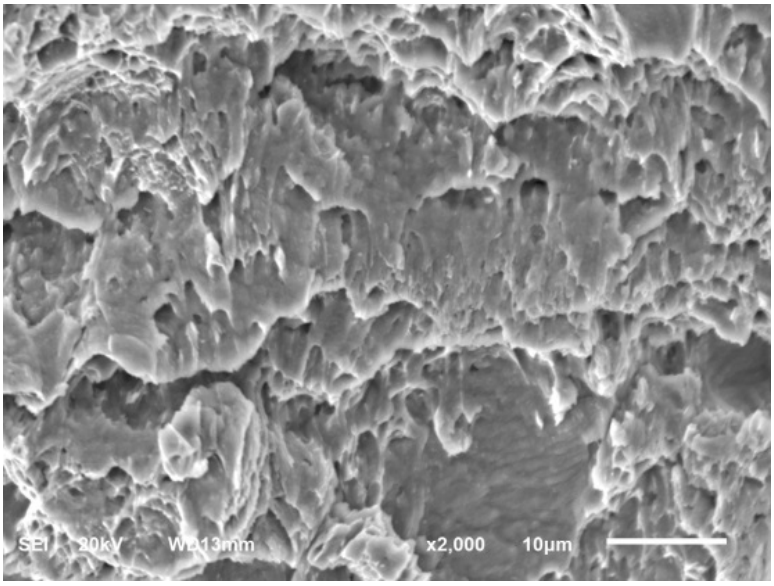

Figure 6: Scanning electron microscopic images of 15-5 PH stainless steel samples test at high temperature (723 K). (2000x magnification. The scale bars represent 10 μm).

4.2.2 Comparison of fracture surface between with modeling results

The fracture surfaces of the broken specimens are compared with the modeling results. A qualitative assessment of both the experimental and numerical modeling indicates that a predominantly brittle failure at 77 K (shown in Fig.7 (a), (b)). The fracture surfaces are almost flat and perpendicular to the tensile direction, indicating a brittle failure as the striker moves through the specimen. Also, the maximum effective plastic strain of 0.451 m/m is the lowest among the three testing temperatures. When tested at room temperature (298 K), the fracture is still brittle (shown in Fig. 7(c), (d)), but the fracture surface is not as flat as the 77 K specimen, indicating that there has been an increase in ductility, and a small portion of the cracks propagates along the 45^{o} maximum shear stress direction. The maximum effective plastic strain of 0.721 m/m is higher than the value at 77 K but lower than that at 723 K. A ductile failure is observed from the specimen

tested at 723 K (shown in Fig. 7 (e), (f)) as the fracture surfaces show a significant level of convexity. Most of the cracks propagate along the maximum shear direction. The effective plastic strain has a maximum value of 1.136 m/m. This represents the highest effective plastic strain, which confirms the highest ductility in three cases.

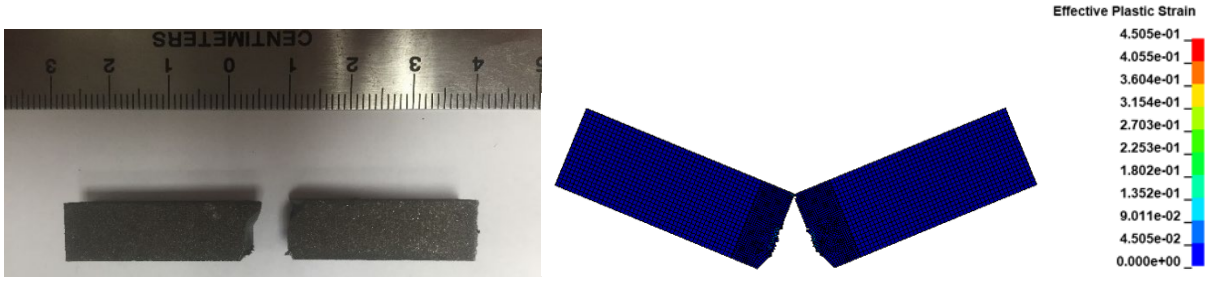

(a) (b)

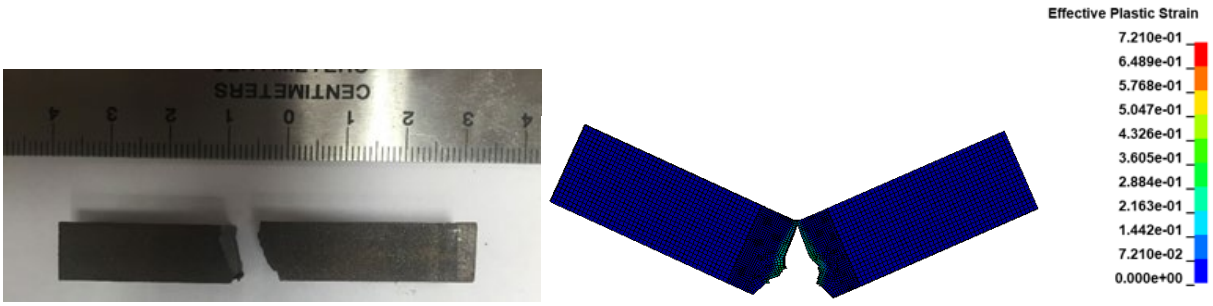

(c) (d)

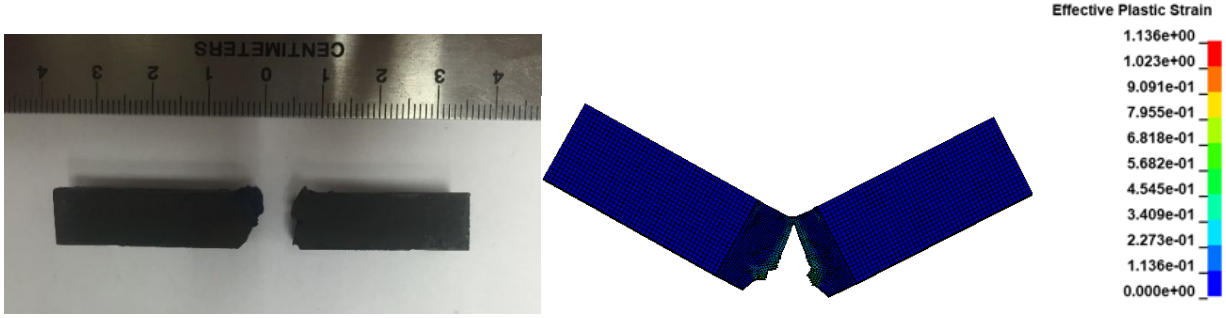

(e) (f)

Figure 7: Fractured specimens from experiment at (a) 77 K, (c) 298 K, and (e) 723 K, and the corresponding simulated effective plastic strain results at (b) 77 K, (d) 298 K, and (f) 723 K.

4.3 Comparison of Charpy impact energy between experiment and modeling results

The experimental tested impact energy at 77 K, 298 K, and 723 K are 0.01 J/cm^2, 6.78±4.07 J/cm^{2,} and 50.84±3.39 J/cm^2 respectively. The numerical modeling results shown in Fig. 8 indicate the impact energy at 77 K, 298 K, and 723 K are 1.05 J/cm^2, 10.46 J/cm^{2,} and 47.07 J/cm^2 respectively.

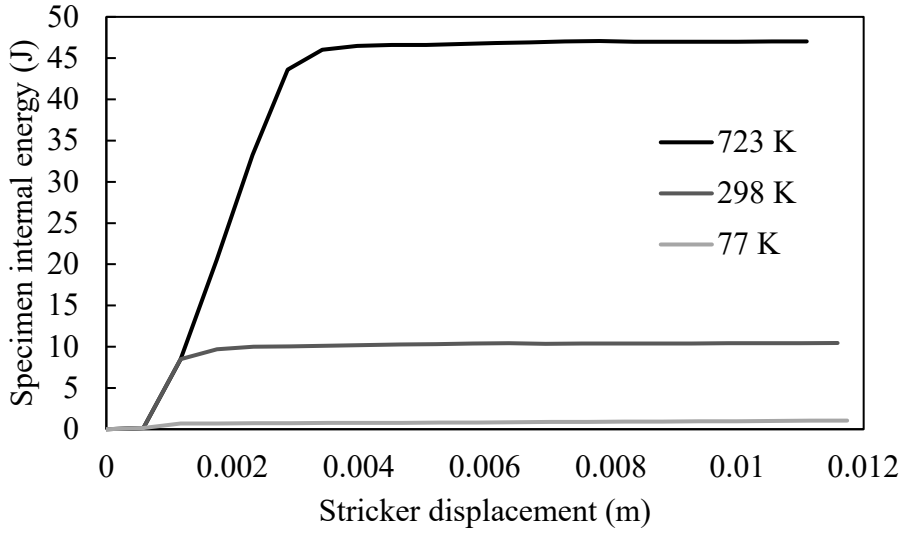

Figure 8: Predicted impact energies as a function of striker displacement at 77 K, 298 K, and 723 K.

Both the experimental and numerical modeling results are in good agreement, as presented in Fig. 9. It indicates a general trend of increasing ductility with the temperature increase. At 77 K, the measured impact energy in the experimental and numerical model were 0.01 J/cm^2 and 1.05 J/cm^2 respectively, which are relatively close to zero. At room temperature and high temperature, the

modeling results are in the same range as that of the experiment data, suggesting the high-fidelity of the finite element model.

It is noted that due to the limited precision of the used impact tester, it is challenging to get a precise measurement at lower temperatures, which have low impact energy. Also, tester settings such as the friction were not fully included in the FE model, which assumed a frictionless contact surface; hence may predict a larger discrepancy between the FE model and experimentally measured values at lower temperatures.

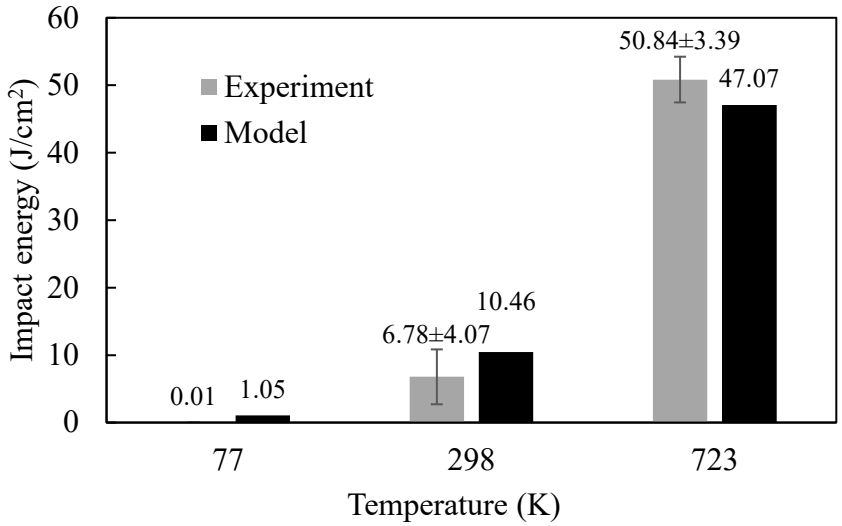

Figure 9: Comparison of impact energy between experimental and numerical modeling.

Our study show that the 3D printed 15-5 stainless steel is generally more brittle than the wrought counterpart, and low impact energy values were acquired both in experiment and modeling (Fig. 9). The brittleness of the printed materials may be because a powder is used as the feedstock in the powder bed fusion 3D printing process. The external defects (pores and unmelted particles) act as sites for crack initiation[22], as shown in Figure 3 in this study. Additionally, the powder may be

exposed to humidity and oxygen, which cause impurity and defects in the printed materials and contribute to their brittleness [19]. A similar low toughness in the Charpy impact test for Ti-6A1-4V, AISI 316L, and maraging steel 300 samples prepared by the selective laser melting (SLM) process was observed. It was attributed to the presence of defects like pores, pick-up of impurities like oxygen and nitrogen especially for titanium alloys, and the presence of more brittle nonequilibrium phases [23]. In the case of aging reported in Ref. [24], Transmission Electron Microscopy (TEM) analysis was conducted to show the formation of fine spherical Cu precipitates in stainless steel, which solution strengthens but makes the specimen brittle [24]. As a result, relatively lower impact toughness is obtained as compared to the overaged condition where a combined effect of coarsening of Cu precipitates and increased retained austenite makes the specimen ductile[24].

5. Conclusions

Charpy impact test was used to investigate the impact properties of 3D printed 15-5 PH stainless steel at three different temperatures. A finite element model based on the phenomenological John-Cook theory was developed to simulate the Charpy test process. The results are summarized below.

1. The experimentally measured impact energies are 0.01 J/cm^2, 6.78±4.07 J/cm^2, and 50.84±3.39 J/cm^2, at the low, room, and high temperatures, respectively.
2. Experimental and numerically modeled impact energy show a good agreement for all three temperatures. The results show a trend of increasing impact energy with increasing temperature, indicating a transition from brittle to ductile failure as the temperature is increased.

3. Fracture surface micrographs show that temperature plays an important role in the impact property of the 3D printed 15-5 PH stainless steel. When tested at low temperature and room temperature, the material showed a brittle behavior with low fracture toughness, as indicated by a transgranular fracture manner. When the specimen was tested at high temperature, the impact energy was significantly increased, and a primarily brittle but with a slightly ductile fracture behavior was observed, as illustrated by a microvoid coalescence induced fracture morphology.

6. Acknowledgments

This work is partially supported by the "Human Resources Program in Energy Technology (No. 20194030202450)", "Power Generation & Electricity Delivery grant (No.20181110100310)" of the Korea Institute of Energy Technology Evaluation and Planning (KETEP), and the National Research Foundation of Korea(NRF) grant funded by the Korea government (MSIP) (2018R1A5A6075959). The authors also thank Prof. David R. Johnson in the School of Materials Engineering at Purdue University for assistance with the Charpy impact tests. S. Sagar is supported by the IUPUI University Diversity Fellowship.

References

[1] Y. Okumoto, Y. Takeda, M. Mano, and T. Okada, *Design of Ship Hull Structures*. 2009.

[2] Y. Zhang *et al.*, "Additive Manufacturing of Metallic Materials: A Review," *Journal of Materials Engineering and Performance,* vol. 27, no. 1, pp. 1-13, 2017.

[3] J. J. Lewandowski and M. Seifi, "Metal Additive Manufacturing: A Review of Mechanical Properties," *Annual Review of Materials Research,* vol. 46, no. 1, pp. 151-186, 2016.

[4] Z. Pitrmuc, "Influence of process parameters and part orientation on mechanical properties for DMLS manufactured Stainless steel AISI 316L," *Conferences of Student Creative Activity, STC 2017,* p. 9, 2017.

[5] J. W. Hendrickson, "Use of Direct Metal Laser Sintering for Tooling in High Volume Production," *All Graduate Plan B and other Reports,* p. 724, 2015.

[6] M. Montero Sistiaga, S. Nardone, C. Hautfenne, and J. Van Humbeeck, "Effect of heat treatment of 316l stainless steel produced by selective laser melting (slm)," *Proceedings of the 27th Annual International Solid Freeform Fabrication Symposium,* pp. 558-565, 2016.

[7] AKSteel, "15-5 PH stainless steel product data bulletin (https://www.aksteel.com/sites/default/files/2018-01/155ph201706.pdf, accessed 3/20/2020)."

[8] E. Herny, P. Lours, E. Andrieu, J. M. Cloué, and P. Lagain, "Evolution of microstructure and impact-strength energy in thermally and thermomechanically aged 15-5 PH," *Proceedings of the Institution of Mechanical Engineers, Part L: Journal of Materials: Design and Applications,* vol. 222, no. 4, pp. 299-304, 2008/10/01 2008.

[9] M. R. Amini, J. Simon, and S. Nemat-Nasser, "Numerical modeling of effect of polyurea on response of steel plates to impulsive loads in direct pressure-pulse experiments," *Mechanics of Materials,* vol. 42, no. 6, pp. 615-627, 2010/06/01/ 2010.

[10] R. Barauskas and A. Abraitienė, "Computational analysis of impact of a bullet against the multilayer fabrics in LS-DYNA," *International Journal of Impact Engineering,* vol. 34, no. 7, pp. 1286-1305, 2007/07/01/ 2007.

[11] "ASTM E23-16b, Standard Test Methods for Notched Bar Impact Testing of Metallic Materials," *ASTM International, West Conshohocken, PA,* 2016.

[12] S. Sagar *et al.*, "Room-Temperature Charpy Impact Property of 3D-Printed 15-5 Stainless Steel," *Journal of Materials Engineering and Performance,* vol. 27, no. 1, pp. 52-56, 2017.

[13] "LS-DYNA," *LSTC,* 2011.

[14] G. R. Johnson and W. H. Cook, "A constitutive model and data for metals subjected to large strains, high strain rates and high temperatures," *Proceedings of the 7th International Symposium on Ballistics,* 1983.

[15] W. T. Graves, D. Liu, and A. N. Palazotto, "Topology Optimization of a Penetrating Warhead," in *57th AIAA/ASCE/AHS/ASC Structures, Structural Dynamics, and Materials Conference*, 2016, p. 1509.

[16] G. R. Johnson and W. H. Cook, "Fracture characteristics of three metals subjected to various strains, strain rates, temperatures and pressures," *Engineering Fracture Mechanics,* vol. 21, no. 1, pp. 31-48, 1985/01/01/ 1985.

[17] A. J. Gross, "Towards the predictive modeling of ductile failure," 2015.

[18] A. Materials. (2013, 03/20). *Stainless Steel - Grade 15-5 PH (UNS S15500)*. Available: https://www.azom.com/article.aspx?ArticleID=8199

[19] K. Coffy, "Microstructure and Chemistry Evaluation of Direct Metal Laser Sintered 15-5 PH Stainless Steel, M.S. thesis," University of Central Florida, 2014.

[20] L. Couturier, F. De Geuser, M. Descoins, and A. Deschamps, "Evolution of the microstructure of a 15-5PH martensitic stainless steel during precipitation hardening heat treatment," *Materials & Design,* vol. 107, pp. 416-425, 2016/10/05/ 2016.

[21] R. W. Hertzberg, R. P. Vinci, and J. L. Hertzberg, *Deformation and Fracture Mechanics of Engineering Materials, 5th Edition*. Wiley, 2012.
[22] Z. Wang *et al.*, "Premature failure of an additively manufactured material," *NPG Asia Materials,* vol. 12, no. 1, p. 30, 2020/04/24 2020.
[23] E. Yasa, J. Deckers, J.-P. Kruth, M. Rombouts, and J. Luyten, "Charpy impact testing of metallic selective laser melting parts," *Virtual and Physical Prototyping,* vol. 5, no. 2, pp. 89-98, 2010/06/01 2010.
[24] S. Sarkar, S. Dubey, and A. K. Nath, "Effect of Heat Treatment on Impact Toughness of Selective Laser Melted Stainless Steel Parts," no. 51357, p. V001T01A005, 2018.